

Metasurface-Enhanced Thermal Photodetector Operating at Gigahertz Frequencies

Eunso Shin, Rachel E. Bangle, Nathaniel C. Wilson, Stefan B. Nikodemski, Jarrett H. Vella, and Maiken H. Mikkelsen*

Thermal photodetectors, including thermoelectric and pyroelectric detectors, are critical for the detection of long-wave infrared light, but they are limited by slow response times due to thermal diffusion. If thermal photodetectors with high speeds and sensitivities can be realized, they would allow for flexible sensing at any wavelength, as all selectivity of the absorber would be reproduced in the detectivity. Here, a room-temperature, pyroelectric photodetector is reported that couples a thermally-sensitive aluminum nitride (AlN) layer with a metallic metasurface that acts as an efficient, spectrally-selective photothermal converter. These pyroelectric detectors exhibit record-breaking speeds, with 3 dB bandwidths up to 2.8 GHz, which corresponds to a rise time of 125 ps. These ultrafast speeds are attained while maintaining competitive responsivities and noise equivalent powers as small as $96 \text{ pW } \sqrt{\text{Hz}^{-1}}$. By varying the active area of devices, it is determined that even the smallest attainable devices are limited by their resistance-capacitance (RC) time constants, and finite element simulations suggest that thermal response times as fast as 30 ps may be realized. These metasurface-enabled pyroelectric photodetectors approach the speeds of commercial semiconductor photodiodes, contrary to the common conception of thermal detectors as slow, and present opportunities for advanced sensing such as spectrally broad multispectral imaging or polarimetry.

generation, they are frequently employed as broadband detectors in the far infrared and microwave regions of the electromagnetic spectrum, where alternative photodetector options are scarce.^[3] Applications of thermal photodetectors outside of the far infrared have been limited, however, due to low sensitivities and long response times, often due to thermal loss to the environment and slow thermal diffusion, respectively.^[4,5] State-of-the-art thermal photodetectors such as photonic cavity-coupled graphene bolometers have achieved ultrafast speeds, with response times as short as 35 ps,^[6,7] but these bolometers offer a trade-off between speed and sensitivity.^[3] While more exotic thermal detectors can achieve high sensitivities with sub- μs response times, they frequently require cryogenic temperatures.^[6,8–10] A graphene bolometer demonstrated a 420 GHz 3 dB bandwidth, though its responsivity was limited to $\sim 400\text{--}500 \text{ } \mu\text{A W}^{-1}$.^[11] An avalanche photodiode achieved a 53 GHz 3 dB bandwidth with a responsivity of 0.87 A W^{-1} .^[12] While these photodetectors have made a significant impact in the field, they still either require external

power or have limitations when it comes to expanding their detection range to broader wavelengths.

Alternatively, pyroelectric detectors are a prominent class of thermal photodetector that generate an electrical signal via heat-induced spontaneous polarization changes within a thermally responsive material.^[13–15] Pyroelectric photodetectors typically operate on millisecond time scales (as summarized in Table S1,

1. Introduction

Thermal photodetectors, which operate through the conversion of absorbed light to heat and the subsequent conversion of this heat to an electrical response, offer wide spectral sensitivity and high damage thresholds.^[1,2] Because thermal detectors can utilize distinct materials for light absorption versus signal

E. Shin, R. E. Bangle, M. H. Mikkelsen
Department of Electrical and Computer Engineering
Duke University
Durham, NC 27703, USA
E-mail: m.mikkelsen@duke.edu
N. C. Wilson, M. H. Mikkelsen
Department of Physics
Duke University
Durham, NC 27703, USA

S. B. Nikodemski
KBR
Beavercreek, OH 45431, USA
J. H. Vella
Sensors Directorate
Air Force Research Laboratory
Wright-Patterson Air Force Base
Dayton, OH 45433, USA

 The ORCID identification number(s) for the author(s) of this article can be found under <https://doi.org/10.1002/adfm.202420953>

DOI: 10.1002/adfm.202420953

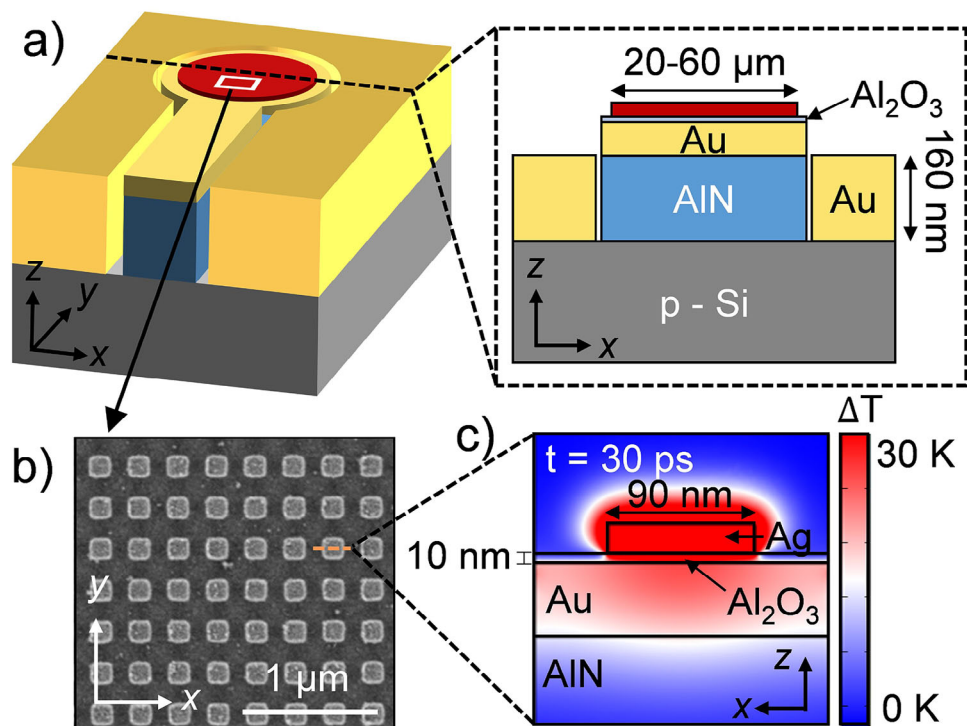


Figure 1. a) Schematic representation of metasurface-enabled photodetectors illustrating key dimensions with b) SEM image of the metasurface absorber. The red area represents the metasurface array. c) Finite element simulations of a single plasmonic nanostructure showing a cross-section of the pyroelectric layer 30 ps after resonant excitation of the metasurface.

Supporting Information), orders of magnitude slower than the nano- to pico-second response times of commercial semiconductor photodiodes.^[1] Though a few examples of conventional pyroelectric photodetectors have demonstrated picosecond response times, this fast operation required unusually powerful laser excitation of >50 kW, unsuitable for practical applications.^[16–18] Recent developments, however, suggest that replacing traditional thick blackened absorbers with nanophotonic absorbers can simultaneously increase sensitivity by imparting spectral selectivity and increase speed by minimizing thermal mass.^[1] Metallic antennas,^[19–21] metallic and dielectric gratings,^[22] and nanoscale hole arrays^[23,24] have been employed to improve the speed and sensitivity of thermal detectors generally, while arrays of film-coupled metallic nanoparticles have allowed for pyroelectric detectors that achieve microsecond-scale response times.^[22] Recently, it was shown that pyroelectric photodetectors paired with a nanogap cavity metasurface absorber exhibited RC limited response times as small as 700 ps, which corresponds to a 500 MHz bandwidth assuming the device operates as a low-pass filter.^[25] The metasurface absorber consisted of colloidal silver nanocubes separated from a flat gold film by a thin (< 10 nm) polymer layer, which acted as a photothermal converter.^[26,27] The small thermal mass of the metasurface absorber led to fast thermal response times, but the ultimate speeds that might be achieved for devices with smaller RC time constants measured with faster readout equipment remained unknown.

Here, we demonstrate a pyroelectric photodetector integrated with a nanogap cavity metasurface sensitive to NIR light. This device exhibits a 2.8 GHz 3 dB bandwidth, corresponding to a 125 ps

rise time, the fastest response time of a pyroelectric photodetector reported to date. In addition, the photodetectors exhibit competitive responsivities and noise equivalent powers, are ultrathin, require no external power or bias, operate at room temperature, and can be readily integrated into on-chip applications. Device bandwidths increase systematically as active areas decrease, and electrical characterization reveals that even the smallest devices are limited by the RC time constants. This creates devices that have response times competitive with those of commercial semiconductor photodiodes and which disprove the frequent supposition that thermal photodetectors must be slow. In addition, the use of precision metasurfaces offers the opportunity to straightforwardly build advanced sensing functionalities such as multi-spectral imaging and polarimetry.^[1,28]

2. Results and Discussion

2.1. Photodetector Design and Fabrication

The metasurface-enabled pyroelectric photodetectors are fabricated by layering a well-established nanogap cavity metasurface structure on top of a pyroelectric thin film (Figure 1). The metallic metasurface consists of an array of nanoscale silver square prisms (90 nm \times 90 nm \times 35 nm) separated from a gold film by a thin dielectric layer, here 10 nm Al_2O_3 , referred to as a “gap” between the metals. The metasurface covered the device’s active area (20 – 60 μm diameter), as illustrated in Figure 1a. This structure acts as an antenna to selectively absorb resonant light nearly completely while reflecting other wavelengths.^[29] The inherent

loss of the plasmonic structures then causes this absorbed energy to be dissipated as heat into the gap on picosecond time scales, which allows the metasurface to simultaneously act as a spectral filter and a photothermal converter.^[25] The heat generated by the metasurface upon light absorption is then transferred through the gold layer to an underlying pyroelectric thin film, here ≈ 160 nm AlN. The AlN layer sandwiched between the gold film of the metasurface and a heavily doped silicon wafer patterned with electrical contacts forms a capacitor. At room temperature, this AlN layer is spontaneously polarized,^[30] which defines the starting capacitance of the structure. Upon heating, the macroscopic dipole moment of the AlN changes, and this change in polarization results in a change in electrical charge at the AlN surface.^[13] This generates a current according to

$$I_p(t) = Ap \frac{dT}{dt} \quad (1)$$

where A is the active area of the device (defined as the illuminated, metasurface-coated area), p is the pyroelectric coefficient, and dT/dt is the change in temperature over time. The AlN thin films employed in this study were previously shown to exhibit x-ray diffraction consistent with preferentially c-axis oriented, polycrystalline materials.^[31] Film thickness was determined by ellipsometry (Figure S1, Supporting Information) to be 160 nm.

Finite element simulations illustrate the operative mechanism of the device and suggest rapid timescales for photothermal conversion and heat dissipation. Absorbed light is converted to heat via oscillatory losses within 5 ps, and the heat reaches the AlN layer within 30 ps (Figure S2, Supporting Information). Heat generation is localized in both the plasmonic mirror and nanostructure according to the relative lossiness of each metal.^[26,27,32] Heat dissipation through the gold to the AlN is then rapid, occurring within 30 ps with dT/dt maximized a mere 4 ps after excitation (Figure S2, Supporting Information). The speed of this thermal transfer, paired with the small thermal mass of the devices, suggests that careful electrical design might result in ultrafast photodetection.

2.2. Photodetector Performance

The near-perfect, spectrally selective absorption of the metasurface, which initiates the photodetector response, is illustrated by white light reflectivity spectra (Figure 2a; Figure S3, Supporting Information). Here, the gold mirror alone efficiently reflects near-infrared light, while the metasurface exhibits a stark relative decrease ($>95\%$) in reflectivity centered at 790 nm. The resonance wavelength is determined by the size of the Ag nanostructures and the thickness of the Al_2O_3 dielectric layer, which allows the possibility of photodetectors that are spectrally selective across the visible and infrared portions of the spectrum.^[25,29,33]

Photodetector responsivities are determined via a lock-in amplifier, which measures the current produced by the device in response to tunable, pulsed laser excitation (100 nW) with the beam size carefully controlled to be ≈ 5 μm smaller than the device diameter, as described in the Experimental Section (Figure 2b). The photocurrent responsivity closely follows the reflectance spectrum, with a maximum peak responsivity of 1.64 mA W^{-1} at

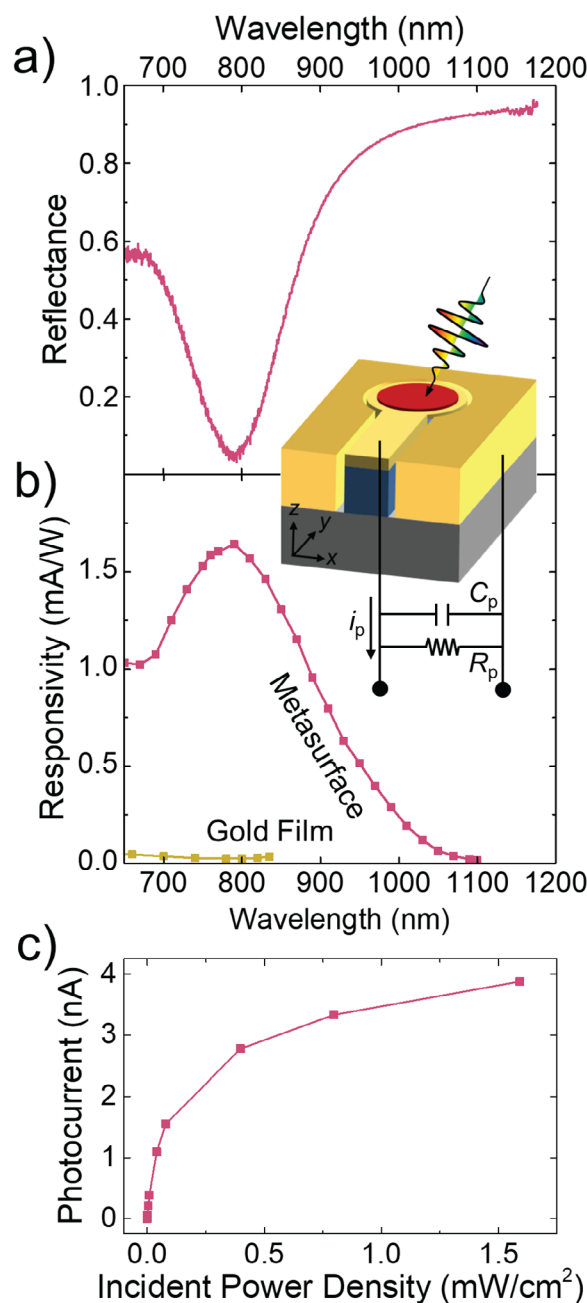


Figure 2. a) White light reflectance spectrum of a detector with a $1.3 \times 10^{-3} \text{ mm}^2$ active area (40 μm diameter). b) Photocurrent responsivity spectra of the detector shown in a) measured upon pulsed 100 nW light excitation as compared to that of a detector in which a gold film rather than a metasurface layer acts as an absorber. c) Photocurrent measured for the device presented in a) and b) upon pulsed 783 nm excitation at the indicated power, with the beam size maintained to consistently have a diameter 5 μm smaller than that of the device.

790 nm for a device with a $1.3 \times 10^{-3} \text{ mm}^2$ active area (40 μm diameter). This is nearly two orders of magnitude larger than the photocurrent responsivity of devices without the metasurface absorber under the same excitation conditions. Noise spectral densities of the detectors are determined with the same lock-in

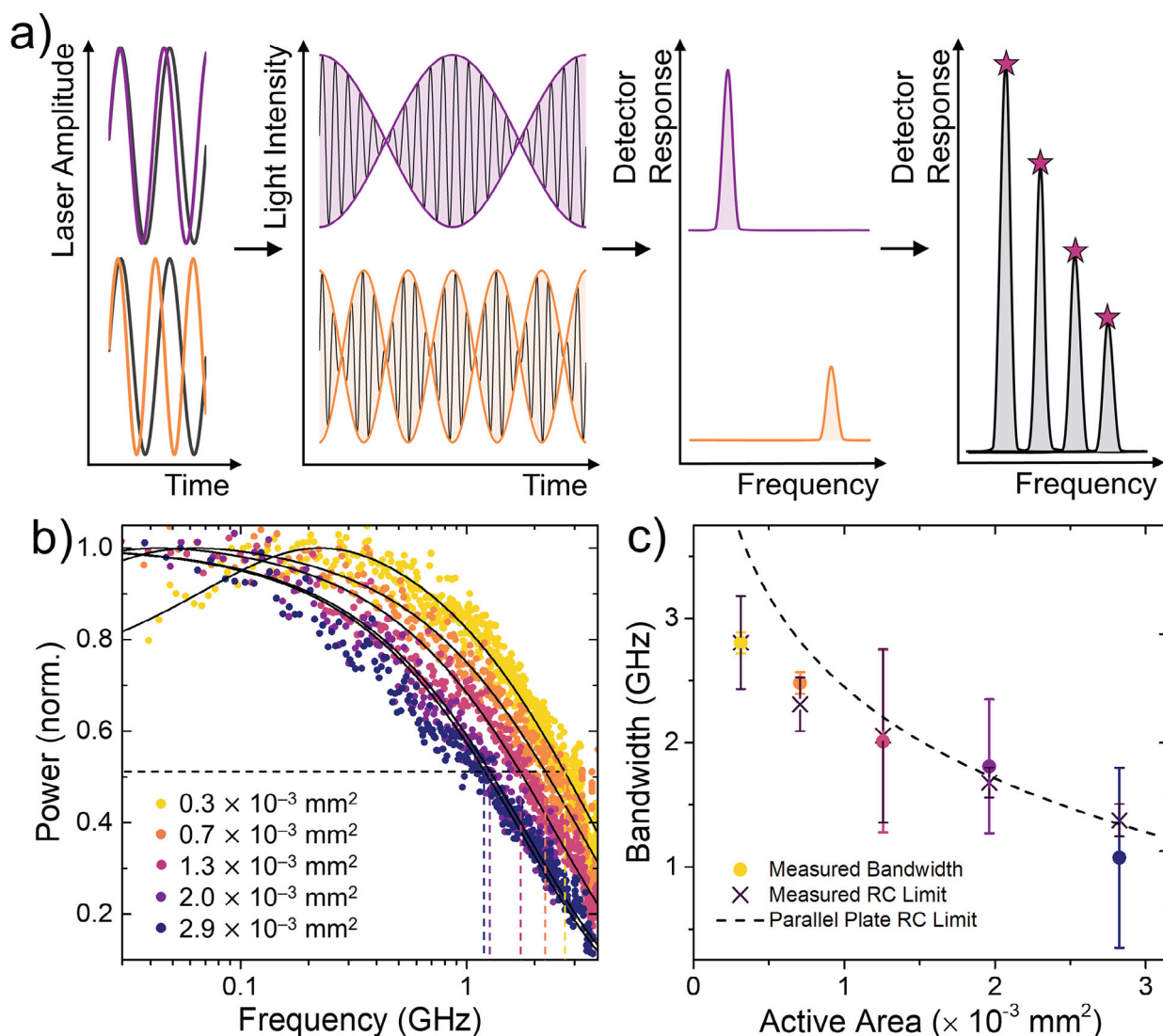


Figure 3. a) Schematic representation of the function of distributed feedback lasers, where two beams with different frequencies interfere to form beat nodes. Detector response decreases as the frequency of the beat node increases to approach the photodetector's ν_{BW} . b) Normalized integrated signal power responses measured as a function of excitation frequencies for devices with the indicated active areas where exponential rise and decay fits determine ν_{BW} . c) Measured values of ν_{BW} extracted from b) (circles) compared to the RC limit derived from measured capacitance values (crosses) and the RC limit predicted for an ideal parallel plate capacitor (dashed line) with the indicated active area.

amplifier, as described in the Methods section, and the noise equivalent power (NEP) is taken as the ratio of the photocurrent responsivity to the noise spectral density (Figure S4c, Supporting Information). For devices with a $1.3 \times 10^{-3} \text{ mm}^2$ active area, photocurrent responsivities upon 790 nm excitation correspond to a NEP as small as $96 \text{ pW } \sqrt{\text{Hz}^{-1}}$. This demonstrates the effectiveness of the metasurface as both a spectral filter and photothermal converter.

The operative photodetector speeds are here quantified as the 3 dB bandwidth (ν_{BW}), which corresponds to the rise time (τ_{rise}) of the device assuming operation as an ideal low-pass filter, as $\nu_{\text{BW}} = 0.35 / \tau_{\text{rise}}$.^[34] Values of ν_{BW} are measured by probing the photodetectors in the frequency domain as described in the Experimental Section. Detectors are resonantly excited (783 nm) with a

sinusoidally modulated laser generated by a pair of distributed feedback lasers, where the modulation frequency corresponds to the beat mode caused by the interference of two beams with offset frequencies.^[35] The frequency of the beat mode is swept from 45 MHz to 4 GHz by tuning the frequency offset of the two beams, and the signal power of the devices is measured as a function of this excitation frequency with a spectrum analyzer (Figure 3). The signal pulse centered at each excitation frequency is integrated to produce a curve of power as a function of excitation frequency, which is fit as an exponential decay to determine ν_{BW} , the frequency at which the signal power response is attenuated by half. The ν_{BW} determined in this manner for a device with a $1.3 \times 10^{-3} \text{ mm}^2$ active area is $2.0 \pm 0.7 \text{ GHz}$, corresponding to $\tau_{\text{rise}} = 175 \text{ ps}$.

Photodetectors with active areas ranging from $2.9 \times 10^{-3} \text{ mm}^2$ to $0.3 \times 10^{-3} \text{ mm}^2$ (60 to 20 μm diameters) are fabricated, and both the photocurrent responsivity spectra and bandwidths are measured. For small devices, optically opaque gold electrical contacts prevent competitive light absorption by the underlying silicon. Devices with $0.3 \times 10^{-3} \text{ mm}^2$ active area represent the smallest devices that can be fabricated using the lithography and etching techniques described in the Experimental Section. For all devices, white light reflectivity spectra demonstrate resonances of $\approx 800 \text{ nm}$, where a small blue shift ($\approx 40 \text{ nm}$) is observed between the largest and smallest detectors (Figure S3, Supporting Information). In addition, the percentage of light absorbed at the resonant wavelength decreases for detectors with active areas $< 1 \times 10^{-3} \text{ mm}^2$, such that the smallest detectors absorb $\approx 60\%$ of resonant light, whereas the largest absorb 98% of resonant light. For all devices, photocurrent responsivity spectra closely follow the reflectivity (Figure 2; Figures S3 and S4a, Supporting Information). As predicted by Equation (1), average photocurrent responsivities under resonant excitation are maximized for the largest measured devices and decrease systematically with smaller active areas, albeit with device-to-device deviations (Figure S4b, Supporting Information). Peak responsivities of $1.23 \pm 0.16 \text{ mA W}^{-1}$ are observed for detectors with $2.9 \times 10^{-3} \text{ mm}^2$ active areas and $0.31 \pm 0.22 \text{ mA W}^{-1}$ for $0.3 \times 10^{-3} \text{ mm}^2$ active areas, which corresponds to average NEP values of 2 and $0.17 \text{ nW Hz}^{-1/2}$, respectively (Figure S4c,d, Supporting Information). Contrary to responsivities, values of ν_{BW} , and thus device speeds, increased for smaller photodetectors, as demonstrated by curves of signal power as a function of excitation frequency (Figure 3b). For devices with $0.3 \times 10^{-3} \text{ mm}^2$ active area, $\nu_{\text{BW}} = 2.80 \pm 0.08 \text{ GHz}$ and thus $\tau_{\text{rise}} = 125 \pm 4 \text{ ps}$.

2.3. Speed Limitations and Future Prospects

Devices are electrically characterized using an impedance analyzer (Keysight KT-E4990A) by measuring their impedance as a function of voltage modulation frequency to determine device capacitance (Methods). These capacitance values are used to quantify the RC time constants of each device. Capacitance values increased systematically with detector active area from 1.1 to 2.4 pF (Figure S5, Supporting Information), which predicts RC-limited bandwidths of $2.8 \pm 0.4 \text{ GHz}$ for the smallest devices. Values of the RC-limited bandwidths align closely with the measured ν_{BW} values, which suggests that even the smallest detectors are RC-limited.

The 2.8 GHz 3 dB bandwidth shown here represents the fastest pyroelectric photodetector reported to date.^[36–38] These ultrafast speeds are attributable to the low thermal mass and small capacitances of the detectors. In a typical case, pyroelectric detectors, and in fact thermal detectors generally, rely on thick blackened absorbers which exhibit spectrally flat responses in the visible and infrared portions of the spectrum.^[13] Though this allows for a broad spectral response, the increased volume results in a large thermal capacitance. This slows the thermal response of the device, in many cases to the point that the thermal response is rate-limiting, resulting in the millisecond response times frequently reported for pyroelectric photodetectors.^[36–39] For the metasurface-enabled detectors reported herein, absorp-

tion is accomplished by nanoscale plasmonic structures, which both lend spectral selectivity and contribute near-negligible thermal mass. This decreases the thermal response time of the devices and imbues spectral selectivity, which results in increased device sensitivity and allows for thinner pyroelectric layers. In total, this results in a device with remarkably small thermal masses and thermal response times significantly shorter than the electrical response times, suggested by finite element simulations to be as short as 30 ps.

Further, high speeds in the devices reported here are in part due to small device capacitances, which are minimized by decreasing the active area. In this way, pyroelectric detectors present a tradeoff between rise time and responsivity, as predicted by the area dependence of the photocurrent and the RC time constant. Low sensitivity of previous pyroelectric detectors has hindered photodetection using small, low-capacitance devices. The photodetectors reported here, however, exhibit measurable responsivities for active areas as small as $0.3 \times 10^{-3} \text{ mm}^2$ (20 μm diameter). While responsivities do follow detector size, even the smallest detectors herein exhibit NEP values $< 10 \text{ nW } \sqrt{\text{Hz}}^{-1}$, which is competitive with much larger detectors in previous generations of analogous devices. In this work, the minimum achievable detector size, and thus the smallest achievable capacitance, was limited by fabrication considerations rather than by responsivity or NEP. Because capacitance is inversely proportional to the distance between the parallel plates, thicker AlN should also decrease the device capacitance. This illustrates a tradeoff between electrical and thermal response times, where total device speeds could be optimized by finding an AlN thickness for which thermal and electrical response times are equal. This would depend on maintaining high device sensitivities and AlN crystal quality across AlN layer thicknesses.

Despite the achieved small capacitances, however, it should be noted that for photodetectors with active area diameters $< \approx 1 \times 10^{-3} \text{ mm}^2$, the measured RC time constants deviated from those predicted for an ideal parallel plate capacitor of equivalent dimensions (Figure 3c). Predicted RC time constants for ideal devices would allow for 3 dB bandwidths up to 3.7 GHz, which would correspond to a rise time of 95 ps. This suggests that deviations from ideal capacitance limit the attainable bandwidths of these metasurface-enabled pyroelectric photodetectors, which likely reflects fabrication defects for the smallest devices. Improved fabrication techniques might present the opportunity to further decrease the electrical response times of these photodetectors and thus increase photodetection speeds further still. Progressively decreased electrical response times within small devices may allow for devices entering the thermally limited regime, where simulations suggest response times could be as small as 30 ps, which would surpass the carrier-limited response times of commercial semiconductor photodiodes. Further, this would enable studies of the fundamental kinetic limits of both thermal conversion within plasmonic nanostructures and depolarization of pyroelectric materials.

The key to realizing these devices, which reach the theoretical maximized pyroelectric detector response times, is thus threefold: 1) maximized sensitivity to allow the greatest range of functional device dimensions, 2) minimized capacitance through small device active areas and optimized AlN thickness, and 3) minimized thermal response times through small thermal

masses. Capacitance and thermal response times offer a trade-off, requiring careful optimization of the pyroelectric layer thickness. Higher sensitivities might be enabled by pyroelectric materials with pyroelectric coefficients larger than that of AlN, such as lithium niobate (LiNbO₃), zinc oxide (ZnO), and zirconium-doped hafnium oxide (HZO).^[40–42] This might be amplified further within the thin pyroelectric layers in these devices, as recent work has shown pyroelectric coefficients to be amplified in very thin layers.^[43] Realization of these optimized devices could enable studies of the fundamental kinetic limits of both thermal conversion within plasmonic nanostructures and depolarization of pyroelectric materials, a practical limitation of pyroelectric photodetector response time in otherwise optimal devices.

3. Conclusion

In this work, metasurface-enabled pyroelectric photodetectors achieve record-breaking 3 dB device bandwidths of 2.8 GHz, corresponding to a rise time of a mere 125 ps. By coupling a nanoscale plasmonic metasurface absorber with a thin pyroelectric AlN film, thermal mass is kept small, and thermal response time is simulated to be only 30 ps. As such, photodetector speeds are found to be limited by the electrical response time, as measured bandwidths closely follow the RC time constants of the devices. These record-breaking speeds are augmented by spectral selectivity conferred by the metasurface absorber/photothermal converter, which can be straightforwardly altered to operate at alternative wavelengths or to add sensitivity to additional light properties such as polarization state.^[24] These photodetectors are ultra-thin, with active layers only 285 nm thick, and small, with active areas as small as $0.3 \times 10^{-3} \text{ mm}^2$, and require no external power or bias to operate. In total, these properties make these devices promising candidates for on-chip photodetection and imaging applications, with potential for scaling to array-based configurations for enhanced performance in large-area sensing and multi-pixel imaging systems.

4. Experimental Section

Pyroelectric Photodetector Fabrication: Photodetectors were fabricated by coupling an electrically active pyroelectric layer with a metallic metasurface acting as a photothermal converter. The pyroelectric layer consisted of $\approx 160 \text{ nm}$ AlN deposited onto highly doped p-type silicon (0-0-1) using vacuum RF sputtering. AlN thicknesses, as reported previously^[28] were measured by ellipsometry (Figure S1, Supporting Information) and verified by SEM imaging a cross-section of the wafer. The silicon wafer was stripped of oxide through submersion in 0.1 M hydrofluoric acid for 1 min prior to deposition. Sputtering was performed with a 5N Al target in an Ar/N₂ atmosphere with the substrate heated to 1000 °C. This process has previously been shown to produce polycrystalline AlN with preferential c-axis orientation, which was verified by X-ray diffraction (Anton Paar XR-Dynamic 500), and $\approx 1 \text{ nm}$ surface roughness. The thickness of AlN was determined through imaging ellipsometry (Accurion EP3).

Devices were patterned from the AlN thin films through a series of metal deposition and lithography steps. First, 5 nm titanium (acting as an adhesion layer) and 75 nm gold were deposited using electron beam evaporation (CHA Industries). Here, the Au layer serves as both a mirror within the nano-gap cavity metasurface and an electrical contact for the device. The Au surface was then spin-coated with a positive photoresist (Microposit Shipley 1813), which was patterned into arrays of devices by covering the device shapes with an opaque photomask and irradiating the exposed

polymer with UV light. The sample was developed (Microposit MF 319) to remove the UV-exposed polymer to create a chemical-resistant mask. The exposed gold was wet etched into the device shape via potassium iodide and iodine chemistry (GE-8110, Transene Company, Inc.), and the remaining resist was removed using Microposit Remover 1165. With the remaining Au acting as a mask, the exposed AlN was etched away in a room temperature aqueous solution of 25% tetramethylammonium hydroxide, alternated with submersion in buffered oxide etch solution. Final electrical contacts were then deposited via electron beam evaporation following patterning to exclude evaporation onto the AlN/Au pillars. Patterning was accomplished with NFR 016D2, which was exposed to UV light and developed in MF 319. A 160 nm layer of Au with a 5 nm Ti adhesion layer was evaporated, and the remaining photoresist was lifted off using Microposit Remover 1165. Though device uniformity could not be directly quantified, device-to-device deviation is reflected in the standard deviations of the RC time constants (Figure 3C).

Metasurfaces were then patterned onto the surface of the device. The Au plane atop the AlN served as a plasmonic mirror. Atomic layer deposition (Cambridge Nanotech Savannah S200) was used to deposit 10 nm aluminum oxide, which served as a dielectric spacer. Metallic nanostructures were then patterned with subsequent electron beam lithography and metal evaporation steps. Electron beam lithography was performed using PMMA A2 resist spun coated to produce a $\approx 75 \text{ nm}$ film into which arrays of $90 \text{ nm} \times 90 \text{ nm}$ squares spaced 100 nm apart were patterned using a 50 pA electron beam (Elonix ELS-7500 EX). After the polymer was developed in a solution of 25% methyl isobutyl ketone in isopropanol, 33 nm Ag with a 3 nm Ti adhesion layer was deposited. The remaining PMMA A2 was dissolved in Microposit Remover 1165 to leave a metallic metasurface with an optical mode at $\approx 780 \text{ nm}$ localized in the Al₂O₃ beneath the Ag nanostructures.

Optical and Electrical Device Characterization: The resonance of the metasurface was determined using reflectivity measurements performed with a home-built microscope as depicted in Figure S6 (Supporting Information) coupled to a spectrometer (Ocean Optics Maya 2000 Pro). White-light reflectivity spectra exhibited characteristic dips corresponding to the near-complete near-infrared absorption by the metasurface. Metasurface spectra were found to be unchanged on the timescale of photocurrent spectra and 3 dB bandwidth measurements (a few hours), though they did exhibit red shifts and spectral broadening characteristic of oxidative degradation of the silver nanostructures after a few months, despite storage in vacuum when devices were not in operation. This degradation might be limited by incorporating protective thin oxide layers to protect from oxygen, though the influence on sensitivity and thermal mass must be further explored.

The responsivity of the devices was measured as a photoinitiated current. The devices were excited using a pulsed supercontinuum laser (NKT Photonics Super K Extreme) coupled with a variable $\approx 10 \text{ nm}$ full-width half-max filter head (SuperK Select). The laser beam was carefully shrunk or expanded to ensure that its diameter (defined as the width of the beam at which the intensity decreases to 1/e of the peak intensity) was $\approx 5 \mu\text{m}$ smaller than that of the device. The laser excitation beam was chopped at a frequency of 3.9 kHz, which was coupled to a lock-in amplifier (Signal Recovery 7265). The resulting current photoresponse of the devices was measured as a function of incident wavelength by the lock-in amplifier to produce photocurrent spectra.

The current response of the devices upon on-resonance excitation (783 nm) was further quantified in the frequency domain to determine the device 3 dB bandwidths (ν_{BW}), defined here as the frequency at which the device response is attenuated by half. Assuming the photodetectors studied here act as an ideal RC low-pass filter, the device rise time (τ_{rise}) can be quantified as $\tau_{\text{rise}} = 0.35/\nu_{\text{BW}}$. To measure ν_{BW} , devices were excited by a sinusoidally modulated 783 nm laser, where rapid modulation was accomplished through the interference of two sinusoidal beams, frequency shifted from each other to produce a beat node. The frequency of the beat was swept by shifting the frequency offset between the interfering beams, and the photocurrent response was measured as a function of this beat frequency from 45 MHz to 4 GHz. To measure photocurrents, devices were coupled to a high-speed, low-noise readout probe (67 GHz

Infinity Probe, GSG), which was coupled to a spectrum analyzer (Tektronix RSA607A). Responsivity peaks at each frequency were integrated to produce curves of response versus excitation frequency and thus determine 3 dB bandwidths.

Device capacitance values were measured using a high-performance impedance analyzer (Keysight E4990A-020). This impedance analyzer used a built-in equivalent circuit model for parallel and serial resistivity (R_p , R_s), inductance (L), and capacitance (C) calculations based on the measured impedance and phase of the device under test (DUT). This measurement showed the detector to have a high parallel resistivity ($R_p \gg 1/\omega C$) and a low inductance (L), satisfying $\omega L \ll 1/\omega C$, where ω is the frequency. Thus, the photodetector was represented using a series C-R-L (Capacitance-Resistance-Inductance) circuit model, and the serial capacitance (C_s) was assumed to be equivalent to the capacitance (C). Based on these measured capacitances, the predicted 3 dB bandwidth of each detector was calculated according to

$$v_{BW} = \frac{1}{2\pi RC} \quad (2)$$

The noise spectrum density (NSD) of the photodetectors was calculated according to

$$NSD = \sqrt{\frac{\sum i_{dark}^2 - \sum i_{short}^2}{N \times 2B}} \quad (3)$$

Here, i_{dark} is the photodetector dark current, i_{short} is the short circuit current, N is 1000, and B is the low-pass filter bandwidth of the lock-in amplifier. Current values were measured by the same lock-in amplifier that is used for measuring responsivity. Values of NSD are used to calculate the photodetector noise equivalent power according to

$$NEP = \frac{NSD}{R(\lambda)} \quad (4)$$

where $R(\lambda)$ is the photodetector responsivity at each incident wavelength.

Finite Element Simulations: Multiphysics simulations of the nanostructures upon illumination were performed using COMSOL Multiphysics with the Wave Optics and Heat Transfer modules. The Wave Optics module was used to calculate the absorption of the single nanostructure upon on-resonance excitation with 780 nm light. This simulated the electromagnetic field distribution within the nanostructure and the absorption magnitude. The incident light is modelled as a Gaussian pulse emulating a picosecond pulsed laser. Nanostructures were then treated as heat sources undergoing resistive power loss within the Heat Transfer module, and temperature changes in the femtosecond and picosecond time regimes were simulated via thermal diffusion.^[26,44] Both modules used the periodic boundary condition applied along the horizontal axes to simulate an array of nanostructures. Along the vertical axis, perfectly matched layer boundary conditions were used to mimic the environment surrounding the nanostructure.

Supporting Information

Supporting Information is available from the Wiley Online Library or from the author.

Acknowledgements

Support is acknowledged from the Air Force Office of Scientific Research (AFOSR MURI, Award # FA9550-21-1-0312). This project is funded in part by the Gordon and Betty Moore Foundation through Grant GBMF8804 to M.H.M. This work was performed in part using instrumentation at the Duke University Shared Materials Instrumentation Facility (SMIF) and the Chapel Hill Analytical and Nanofabrication Laboratory (CHANL). Both

SMIF and CHANL are members of the North Carolina Research Triangle Nanotechnology Network (RTNN), which is supported by the National Science Foundation (Grant ECCS-1542015), as part of the National Nanotechnology Coordinated Infrastructure (NNCI). This material is based on work supported by the Air Force Research Laboratory under award FA807518D0015 (S.N.).

Conflict of Interest

The authors declare no conflict of interest.

Data Availability Statement

The data that support the findings of this study are available from the corresponding author upon reasonable request.

Keywords

aluminum nitride, metasurface, photodetector, plasmonics, pyroelectricity

Received: October 31, 2024

Revised: April 14, 2025

Published online:

- [1] J. W. Stewart, N. C. Wilson, M. H. Mikkelsen, *ACS Photonics* **2021**, *8*, 71.
- [2] A. Rogalski, *Prog. Quantum Electron.* **2003**, *27*, 59.
- [3] U. Sassi, R. Parret, S. Nanot, M. Bruna, S. Borini, D. De Fazio, Z. Zhao, E. Lidorikis, F. H. L. Koppens, A. C. Ferrari, A. Colli, *Nat. Commun.* **2017**, *8*, 14311.
- [4] J. J. Talghader, A. S. Gawarikar, R. P. Shea, *Light Sci. Appl.* **2012**, *1*, 24.
- [5] R. W. Whatmore, S. J. Ward, *J. Appl. Phys.* **2023**, *133*, 080902.
- [6] D. K. Efetov, R.-J. Shiue, Y. Gao, B. Skinner, E. D. Walsh, H. Choi, J. Zheng, C. Tan, G. Grosso, C. Peng, J. Hone, K. C. Fong, D. Englund, *Nat. Nanotechnol.* **2018**, *13*, 797.
- [7] X. Gan, R. J. Shiue, Y. Gao, I. Meric, T. F. Heinz, K. Shepard, J. Hone, S. Assefa, D. Englund, *Nat. Photonics* **2013**, *7*, 883.
- [8] G.-H. Lee, D. K. Efetov, W. Jung, L. Ranzani, E. D. Walsh, T. A. Ohki, T. Taniguchi, K. Watanabe, P. Kim, D. Englund, K. C. Fong, *Nature* **2020**, *586*, 42.
- [9] G. Skoblin, J. Sun, A. Yurgens, *Appl. Phys. Lett.* **2018**, *112*, 063501.
- [10] Z. Hu, L. Zhang, A. Chakraborty, G. D'Olimpio, J. Fujii, A. Ge, Y. Zhou, C. Liu, A. Agarwal, I. Vobornik, D. Farias, C. N. Kuo, C. S. Lue, A. Politano, S. W. Wang, W. Hu, X. Chen, W. Lu, L. Wang, *Adv. Mater.* **2023**, *35*, <https://doi.org/10.1002/adma.202209557>.
- [11] S. M. Koepfli, M. Baumann, R. Gadola, S. Nashashibi, Y. Koyaz, D. Rieben, A. C. Güngör, M. Doderer, K. Keller, Y. Fedoryshyn, J. Leuthold, *Nat. Commun.* **2024**, *15*, 7351.
- [12] Y. Shi, X. Li, G. Chen, M. Zou, H. Cai, Y. Yu, X. Zhang, *Nat. Photonics* **2024**, *18*, 610.
- [13] S. B. Lang, *Phys. Today* **2005**, *58*, 31.
- [14] B. Szigeti, *Phys. Rev. Lett.* **1975**, *35*, 1532.
- [15] J. H. Goldsmith, S. Vangala, J. R. Hendrickson, J. W. Cleary, J. H. Vella, *J. Opt. Soc. Am. B* **2017**, *34*, 1965.
- [16] S. C. Stotlar, E. J. McLellan, A. J. Gibbs, J. Webb, *Proc. SPIE 0190*, Los Alamos Conference on Optics 1979, **1980**, <https://doi.org/10.1117/12.957770>.
- [17] C. B. Roundy, *Proc. SPIE 0062*, Modern Utilization of Infrared Technology, **1976**, <https://doi.org/10.1117/12.954450>.

- [18] C. B. Roundy, R. L. Byer, D. W. Phillion, D. J. Kuizenga, *Opt. Commun.* **1974**, *10*, 374.
- [19] S. A. Kuznetsov, A. G. Paulish, M. Navarro-Cía, A. V. Arzhannikov, *Sci. Rep.* **2016**, *6*, 21079.
- [20] X. Tan, J. Li, A. Yang, H. Liu, F. Yi, Proc. SPIE OPTO, Smart Photonic Optoelectron. Integr. Circuits XX, **2018**, <https://doi.org/10.1117/12.2286437>.
- [21] J. Y. Suen, K. Fan, J. Montoya, C. Bingham, V. Stenger, S. Sriram, W. J. Padilla, *Optica* **2017**, *4*, 276.
- [22] T. D. Dao, S. Ishii, A. T. Doan, Y. Wada, A. Ohi, T. Nabatame, T. Nagao, *Adv. Sci.* **2019**, *6*, 1900579.
- [23] K. Yamamoto, F. Goericke, A. Guedes, G. Jaramillo, T. Hada, A. P. Pisano, D. Horsley, *Appl. Phys. Lett.* **2014**, *104*, 111111.
- [24] T. D. Dao, S. Ishii, T. Yokoyama, T. Sawada, R. P. Sugavaneshwar, K. Chen, Y. Wada, T. Nabatame, T. Nagao, *ACS Photonics* **2016**, *3*, 1271.
- [25] J. W. Stewart, J. H. Vella, W. Li, S. Fan, M. H. Mikkelsen, *Nat. Mater.* **2020**, *19*, 158.
- [26] J. W. Stewart, T. Nebabu, M. H. Mikkelsen, *Nano Lett.* **2022**, *22*, 5151.
- [27] X. Cui, Q. Ruan, X. Zhuo, X. Xia, J. Hu, R. Fu, Y. Li, J. Wang, H. Xu, *Chem. Rev.* **2023**, *123*, 6891.
- [28] N. C. Wilson, E. Shin, R. E. Bangle, S. B. Nikodemski, J. H. Vella, M. H. Mikkelsen, *Nano Lett.* **2023**, *23*, 8547.
- [29] G. M. Akselrod, J. Huang, T. B. Hoang, P. T. Bowen, L. Su, D. R. Smith, M. H. Mikkelsen, *Adv. Mater.* **2015**, *27*, 8028.
- [30] N. Li, C. P. Ho, S. Zhu, Y. H. Fu, Y. Zhu, L. Y. T. Lee, *Nanophotonics* **2021**, *10*, 2347.
- [31] N. C. Wilson, E. Shin, R. E. Bangle, S. B. Nikodemski, J. H. Vella, M. H. Mikkelsen, *Nano Lett.* **2023**, *23*, 8547.
- [32] M. R. Bourgeois, F. Pan, C. P. Anyanwu, A. G. Nixon, E. K. Beutler, J. A. Dionne, R. H. Goldsmith, D. J. Masiello, *Annu. Rev. Phys. Chem.* **2024**, *75*, 509.
- [33] J. W. Stewart, G. M. Akselrod, D. R. Smith, M. H. Mikkelsen, *Adv. Mater.* **2017**, *29*, 1602971.
- [34] E. Bogatin, *Signal and Power Integrity-Simplified*, Prentice Hall, Ann Arbor, Michigan, **2004**.
- [35] S. Kraft, A. Deninger, C. Trüch, J. Fortágh, F. Lison, C. Zimmermann, *Laser Phys. Lett.* **2005**, *2*, 71.
- [36] L. Wang, H. Xue, M. Zhu, Y. Gao, Z. Wang, *Nano Energy* **2022**, *97*, 107163.
- [37] Y. Zhang, M. Hu, Z. Wang, *Nano Energy* **2020**, *71*, 104630.
- [38] Y. Chang, J. Wang, F. Wu, W. Tian, W. Zhai, *Adv. Funct. Mater.* **2020**, *30*, 2001450.
- [39] S. Ebrahim, A. M. Elshaer, M. Soliman, M. B. Tayl, *Sensors Actuators A Phys* **2016**, *238*, 389.
- [40] M. Kumar, H. Seo, *Adv. Mater.* **2022**, *34*, 2106881.
- [41] J. Tian, *AIP Adv.* **2023**, *13*, 050701.
- [42] S. Bhowmick, M. Iodice, M. Gioffrè, G. Breglio, A. Irace, M. Riccio, G. Romano, S. Grilli, P. Ferraro, L. Mecozzi, S. Coppola, O. Gennari, R. Rega, G. Coppola, *Sensors Actuators, A Phys* **2017**, *261*, 140.
- [43] J. Jiang, L. Zhang, C. Ming, H. Zhou, P. Bose, Y. Guo, Y. Hu, B. Wang, Z. Chen, R. Jia, S. Pendse, Y. Xiang, Y. Xia, Z. Lu, X. Wen, Y. Cai, C. Sun, G.-C. Wang, T.-M. Lu, D. Gall, Y.-Y. Sun, N. Koratkar, E. Fohntung, Y. Shi, J. Shi, *Nature* **2022**, *607*, 480.
- [44] X. T. Kong, L. Khosravi Khorashad, Z. Wang, A. O. Govorov, *Nano Lett.* **2018**, *18*, 2018.